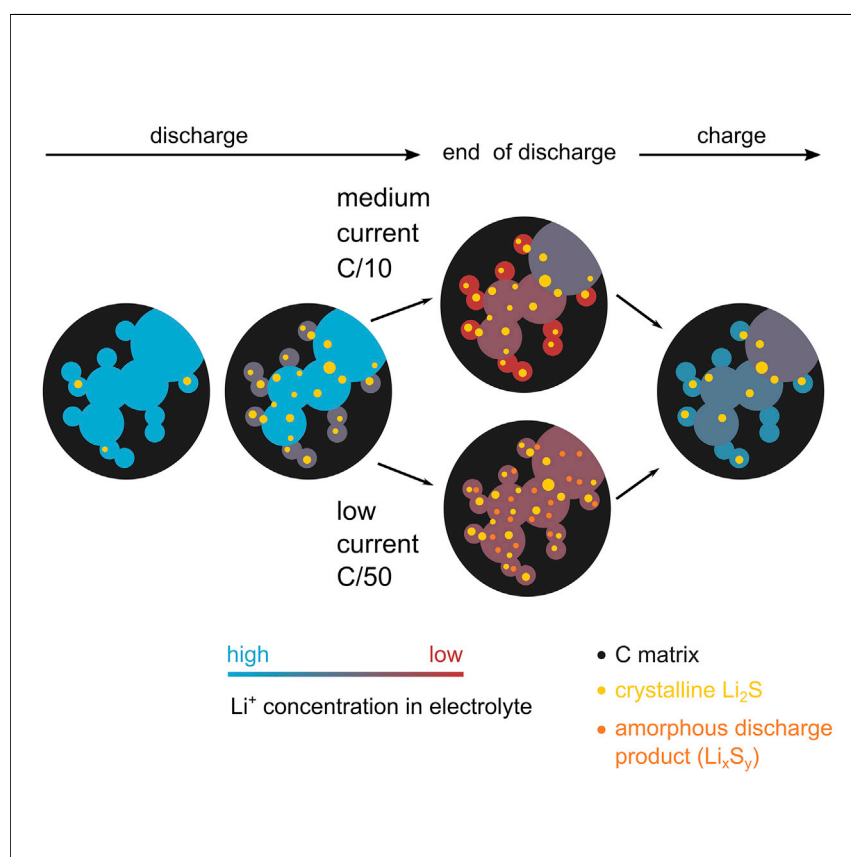


Article

Correlations between precipitation reactions and electrochemical performance of lithium-sulfur batteries probed by *operando* scattering techniques

On the second discharge voltage plateau of a Li-S battery, solid discharge product precipitates from the intermediates dissolved in the electrolyte in the porous carbon matrix of the positive electrode. The low realized capacity compared with the theoretical value stems from the low sulfur utilization at this stage. Using *operando* scattering techniques in multiple contrasts, this work characterizes the changes in multiple phases simultaneously and demonstrates the limiting factors for the discharge capacity at different currents.

Yu-Chuan Chien, Matthew J. Lacey, Nina-Juliane Steinke, Daniel Brandell, Adrian R. Rennie

daniel.brandell@kemi.uu.se (D.B.)
adrian.rennie@kemi.uu.se (A.R.R.)

Highlights

Small- and wide-angle scattering techniques with neutron and X-ray are applied

Scattering in multiple contrasts resolves the discharge process of Li-S batteries

Amorphous discharge product is found at low current

Results suggest that Li⁺ transport limits the discharge process at medium current

Article

Correlations between precipitation reactions and electrochemical performance of lithium-sulfur batteries probed by *operando* scattering techniques

Yu-Chuan Chien,¹ Matthew J. Lacey,² Nina-Juliane Steinke,³ Daniel Brandell,^{1,5,*} and Adrian R. Rennie^{4,*}

SUMMARY

A comprehensive description of electrochemical processes in the positive electrode of lithium-sulfur batteries is crucial for the utilization of active material. However, the discharge mechanisms are complicated due to various reactions in multiple phases and the tortuosity of the highly porous carbon matrix. In this work, simultaneous measurements of small-angle and wide-angle scattering and cell resistance are performed on operating lithium-sulfur cells. Results indicate that precipitates grow mostly in number, not in size, and that the structure of the carbon matrix is not affected. The comparison of the small-angle and wide-angle scattering reveals the amorphous discharge products found at a low discharge rate. Further analysis demonstrates the correlation between the diffusion resistance and the compositional change of electrolyte in the mesopores at the end of discharge, which suggests that Li-ion deficiency is the limiting factor for sulfur utilization at a medium discharge rate.

INTRODUCTION

Much expectation and thus research attention have been placed on lithium-sulfur (Li-S) batteries because of their high theoretical specific energy (2,552 Wh kg⁻¹)¹ on the materials level and the availability of sulfur as a by-product of oil refinement.² However, the low utilization of sulfur and the low reversibility of metallic lithium limit the specific energy density to around 400 Wh kg⁻¹ on the cell level so far.^{3–5} Moreover, the reactions between the reactive lithium anode and the catholyte, i.e., cathode materials dissolved in an electrolyte, result in self-discharge and thus low Coulombic efficiency.⁶

The low sulfur utilization, which is reflected by the ratio between the realized and theoretical specific capacity of the positive electrode expressed per unit mass of sulfur (1,672 mA h g⁻¹),¹ stems from the complex reaction mechanism at the positive electrode.^{1,7} On discharge, elemental sulfur is reduced to various reaction intermediates, e.g., lithium polysulfides (Li₂S_x, x = 2–8), which are soluble in the widely adopted ether-based electrolytes.⁸ As the cell continues to discharge, lithium polysulfides are further reduced to lithium sulfide (Li₂S). The reactions are reversed upon charging, but the exact species of polysulfides differ.⁹ Since sulfur and Li₂S are insoluble, both dissolution and precipitation occur during discharge or charge. Moreover, owing to their low electronic conductivity, a porous conductive matrix with high specific surface area, usually made from carbon, is required to facilitate the electrochemical reactions.^{2,10} Therefore, understanding the interplay between the formation of the insulating species and the functionality of the carbon matrix is critical to the improvement of sulfur utilization.

The bigger picture

While lithium-sulfur batteries are regarded as one of the promising energy storage systems for the future, the specific energy demonstrated so far (~400 Wh kg⁻¹) is severely hampered by the low utilization of active materials in both the positive and negative electrodes. In this context, the incomplete discharge process at the positive electrode has been associated with precipitation of insulating final products from the soluble intermediates, which occurs by a process that is largely unclear. A mechanistic understanding of these multiphase reactions in an operating electrode is however essential to improve the system. Through a combination of scattering measurements using different contrasts, this work identifies not only the crystalline solids but also the amorphous product and the compositional variation of the electrolyte in the porous electrode. With simultaneously measured cell resistance, limitations of the discharge capacity are identified to guide further development.

While the precipitation and dissolution of elemental sulfur are characterized to be fast and reversible processes,^{11,12} the formation of Li_2S is often blamed for limiting sulfur utilization due to the larger volume per sulfur atom. Assuming all the elemental sulfur is converted to form Li_2S , an increase of approximately 20% in volume has to be accommodated in the carbon matrix, which can substantially decrease the volume fraction of the electrolyte inside the pores even if the reaction is not complete. In addition to pore blocking, the insulating precipitate is also reported to passivate the conductive porous matrix,^{13,14} although some studies suggest that the passivation is not limiting in thin electrodes with high electrolyte-to-sulfur ratio.¹⁵ Nevertheless, there is a consensus that the incomplete formation of Li_2S is a roadblock to approaching the theoretical specific capacity. Consequently, the precipitation of Li_2S has been investigated extensively in recent studies.^{16–22}

The reports on Li_2S formation can be categorized into characterization of the bulk electrode and studies of the electrode surface. With cell modifications, the Li_2S formation in bulk electrodes is often probed by X-ray diffraction (XRD) and/or imaging during cell operation. It was, for example, observed using *operando* diffraction that the rate of increase of the intensity from the crystalline Li_2S reduces while a constant discharge current is applied, so other non-crystalline or amorphous sulfur species, such as Li_2S_2 , must be formed during the later stage of discharge.¹⁶ The dependence of the morphology of Li_2S on temperature, current density, and state of charge has also been characterized by *operando* XRD and radiography.¹⁸ The impact of Li_2S on the transport properties of the carbon matrix was moreover demonstrated by coupling diffraction with real-time resistance measurements.¹⁹ In contrast, the Li_2S precipitates on the electrode surface are usually revealed by post-mortem scanning electron microscopy (SEM), though an *operando* morphological study has been conducted with atomic force microscopy.²⁰ Higher resolution of the SEM images provides detailed morphology for kinetic studies.^{21,22} Despite this variety, each technique has some of its own respective drawbacks in identification of the limiting factor for the discharge process. The *operando* XRD, for example, cannot detect amorphous solids, while the X-ray imaging has limited spatial resolution. The post-mortem analyses often risk discrepancies caused by the cell disassembly and sample preparation. Moreover, the observation on an electrode surface may not reflect the precipitation within a tortuous carbon matrix.

Small-angle scattering provides the possibility of morphological characterization of both crystalline and amorphous solid discharge products in an operational Li-S cell. Small-angle X-ray scattering (SAXS) has been applied widely to probe the pore structure of carbonaceous materials,^{23,24} as well as to characterize the impregnation of sulfur into the pores.^{25,26} Small-angle neutron scattering (SANS) has been used to reveal the different morphologies of the precipitate in a carbon matrix in lithium-oxygen batteries,²⁷ which possess similarities to the Li-S system. While SAXS is more accessible, SANS measurements benefit from the adjustable contrast in terms of different scattering length densities (SLDs) obtained through deuteration of solvents. Recently, *operando* SANS studies have been conducted on Li-S batteries. Risse et al.²⁸ characterized the precipitation behavior of sulfur and Li_2S in a deuterated catholyte cell with microporous carbon cloth and reported that the Li_2S does not form inside the micropores. Jafta et al.²⁹ employed a similar microporous carbon cloth electrode to study the influence of different sulfur infiltration methods and performed *operando* SANS with a sulfur-infiltrated carbon matrix and a hydrogenous electrolyte, from which the authors concluded that Li_2S precipitates inside the micropores. The contradictory results suggest that more information is required to elucidate the full picture.

¹Department of Chemistry-Ångström Laboratory, Uppsala University, Box 538, Lägerhyddsvägen 1, 75121 Uppsala, Sweden

²Scania CV AB, 151 87 Södertälje, Sweden

³Institut Laue-Langevin, 71 Avenue des Martyrs, CS 20156, 38042 Grenoble, Cedex 9 France

⁴Centre for Neutron Scattering, Uppsala University, Box 516, 75121 Uppsala, Sweden

⁵Lead contact

*Correspondence:
daniel.brandell@kemi.uu.se (D.B.),
adrian.rennie@kemi.uu.se (A.R.R.)

<https://doi.org/10.1016/j.chempr.2022.03.001>

Table 1. Cell parameters of the *operando* SANS and SAXS cells

Cell	Electrolyte solvent	e/S/ $\mu\text{L mgs}^{-1}$	S-loading/ mgs cm^{-2}	Electrode thickness/ μm
SANS-D	d-DME:d-THF 1:1, v:v	8	3.93	116
SANS-H	DME:THF 1:1, v:v	8	4.08	124
SAXS	DME:DOL 1:1, v:v	6	3.06	67

Please refer to section “materials” for the acronyms of the solvents. The electrolyte-sulfur (e/S) ratio is expressed with respect to the mass of sulfur in milligrams (mgs). The thickness of the electrode coating is measured by disassembling the cells after the small-angle scattering measurements.

In this work, *operando* measurements of SAXS and SANS with both deuterated and hydrogenous electrolytes are carried out on a previously optimized sulfur-carbon composite electrode³⁰ with a mesoporous carbon host to probe the precipitation process of Li_2S in three different contrasts. Use of multiple contrast conditions that exploit the different scattering of hydrogen and deuterium isotopes in neutron experiments together with comparable X-ray data allows identification of particular materials that change and contribute to the observed results. The scattering data are fitted with a simple two-sphere model, which renders a consistent set of parameters across the SANS data with deuterated electrolyte, SAXS data, and the concurrent wide-angle X-ray scattering (WAXS) measurements. The lack of variation in the SANS data from the cell with hydrogenous electrolyte also indicates the medium where Li_2S precipitates. With the simultaneous resistance measurements enabled by the intermittent current interruption (ICI) method,^{19,31} a comprehensive picture as to how the discharge process is limited under various current densities can thereby be presented. This approach using multiple measurements of scattering provides specific insights as described below.

RESULTS AND DISCUSSION

Three modified coin cells were fabricated for *operando* scattering measurements with both X-ray and neutrons. Both deuterated and hydrogenous electrolytes are used for SANS in cells, i.e., SANS-D and SANS-H, respectively. The details of the cell components can be found in Table 1.

Comparison between the raw scattering data in three contrasts

The azimuthally averaged scattering data for the SANS-D, SANS-H, and SAXS cells at selected states of discharge or charge in the first cycle are shown in Figure 1. The Bragg reflection contributed by the polyimide can be observed around 0.4 \AA^{-1} in all four plots, which is confirmed by the measurements of scattering from the individual cell components shown in Figure S1. While the variation in the scattering curves of the SANS-D cell is obvious, the change in scattering from the SANS-H cell is minimal across all the states of charge. This large difference between the two SANS cells can be attributed to the different electrolyte. Assuming that the morphology and distribution of the precipitates are identical for the deuterated and hydrogenous electrolyte, the change in intensity will be proportional to the square of the SLD difference between Li_2S and the respective electrolyte. As tabulated in Table 2 and illustrated in Figure S3, the SLD of the Li_2S is very close to that of the hydrogenous electrolyte but far from that of the deuterated electrolyte. The similarity of all the scattering curves of the SANS-H cell indicates that the structure of the carbon matrix is not altered by the precipitates, i.e., they replace the electrolyte, most likely in the pores of the carbon based on the previous post-mortem scanning electron microscopic reports.¹⁵

The changes in the scattering curves of the SAXS cell are noticeable but not as substantial as those of the SANS-D cell. This is a consequence of the smaller contrast

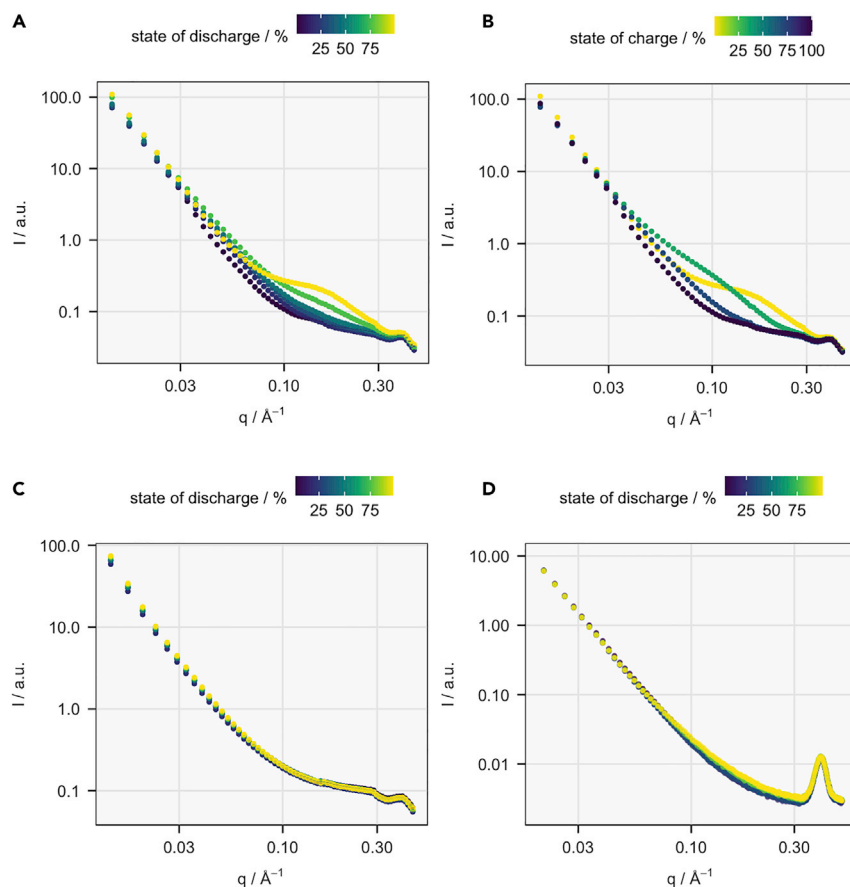


Figure 1. Azimuthally averaged small-angle scattering data from the first cycle of operando measurements

Selected data from the first discharge of the cells (A) SANS-D, (C) SANS-H, and (D) SAXS and (B) the first charge of the SANS-D cell demonstrate the trends of scattering intensity as the cells discharge or charge. The intensity (I) is plotted against the momentum transfer (q) while the state of discharge or charge is shown by the color. The measurements of the SANS-H and SAXS cells during the first charge are shown in Figure S2.

between the electrolyte and Li_2S than that between the electrolyte and the carbon matrix, as shown in Table 2 and Figure S3. Nevertheless, since the SAXS measurements are normalized to the transmission, the variations are still significant when the background is subtracted, as demonstrated in the following section. In addition, the analyses can be verified by the WAXS data that are measured concurrently.

Comparison of the background-subtracted data

To eliminate the scattering contribution from other components of the cell during further analysis of SANS-D and SAXS cells, the first scattering curve is subtracted from the following ones, of which the examples are displayed in Figure 2. Since negative values result from the subtraction for the SAXS data, the square of the intensity is also plotted in the logarithmic scale in Figure 2C for easier comparison with Figure 2A. Due to the anisotropy of scattering caused by the separator for $q < 0.03 \text{ \AA}^{-1}$ from the data of the SANS-D cell, the following analysis will be limited to $q > 0.03 \text{ \AA}^{-1}$. Data from both the cells show that there are two ranges where there are intensity differences: ΔI , one is around 0.04 \AA^{-1} and the other is around 0.2 \AA^{-1} . Both are positive in SANS, but the former is negative in SAXS, which indicates that

Table 2. Calculation of the scattering length density (SLD) from the measured density

Substance	Chemical formula	Formula mass	Density/g cm ⁻³	X-ray SLD/10 ⁻⁶ Å ⁻¹	Neutron SLD/10 ⁻⁶ Å ⁻¹
Carbon	C		2.0	17	6.7
α-S	S		2.07	17.9	1.11
β-S	S		1.96	16.9	1.05
Li ₂ S	Li ₂ S		1.66	13.8	-0.21
Hydrogenous electrolyte	C ₂ F ₆ LiNO ₄ S ₂ (LiNO ₃) _{0.25} (C ₄ H ₁₀ O ₂) _{5.56} (C ₄ H ₈ O) _{6.94}	1305.8	1.0227		0.525
Hydrogenous electrolyte with Li ₂ S ₆ (e/S = 8)	C ₂ F ₆ LiNO ₄ S ₂ (LiNO ₃) _{0.25} (C ₄ H ₁₀ O ₂) _{5.56} (C ₄ H ₈ O) _{6.94} Li _{1.66} S _{4.98}	1477.0	1.1051		0.552
Deuterated electrolyte	C ₂ F ₆ LiNO ₄ S ₂ (LiNO ₃) _{0.25} (C ₄ D ₁₀ O ₂) _{5.56} (C ₄ D ₈ O) _{6.94}	1417.7	1.1103		5.98
Deuterated electrolyte with Li ₂ S ₆ (e/S = 8)	C ₂ F ₆ LiNO ₄ S ₂ (LiNO ₃) _{0.25} (C ₄ D ₁₀ O ₂) _{5.56} (C ₄ D ₈ O) _{6.94} Li _{1.66} S _{4.98}	1588.9	1.1888		5.77
Electrolyte (SAXS)	C ₂ F ₆ LiNO ₄ S ₂ (LiNO ₃) _{0.25} (C ₄ H ₁₀ O ₂) _{4.99} (C ₃ H ₆ O ₂) _{7.42}		1.1207	10.2	
Electrolyte (SAXS) with Li ₂ S ₆ (e/S = 6)	C ₂ F ₆ LiNO ₄ S ₂ (LiNO ₃) _{0.25} (C ₄ H ₁₀ O ₂) _{4.99} (C ₃ H ₆ O ₂) _{7.42} Li _{1.66} S _{4.98}		1.2117	10.9	

Calculations are carried out with the neutron activation and scattering calculator of the National Institute of Standards and Technology (NIST), United States. (<https://www.ncnr.nist.gov/resources/activation/>) The densities of the two hydrogenous electrolytes, with and without Li₂S₆, are measured by a density meter (Anton Paar model 4500). The densities of the deuterated electrolytes are scaled by their formula mass. The estimate of the scattering length density of the deuterated electrolyte is based on the same molarity of the electrolyte salts; the molality counterpart is slightly lower than the actual molality counterpart of the salts in the electrolyte. However, the trend in scattering length density would be similar. The values that are irrelevant to the calculation or data analysis are left blank in the table.

they arise from different processes. Since the precipitation of Li₂S does not decrease the scattering intensity, the contribution at lower q must stem from another phenomenon. Therefore, it is reasonable to apply a model with two separate distributions of objects, taken as spheres, to fit the data. The interpretation of the different contributions to scattering variation will be described further with the results of fits.

Application and interpretation of the two-sphere model

The intensity differences for the SANS-D and SAXS cells are fitted by a two-sphere model described by Equations 1, 2, 3, and 4, which is the addition of scattering from two independent distributions of spherical objects (A and B in the following equation) with polydispersity.

$$\Delta I(q) = \sum_{i=A,B} \int_0^\infty f(r_i, r_{med,i}, \sigma_i) \frac{(scale)_i (\Delta\rho_i)^2}{V_i} \left[3V_i \frac{\sin(qr_i) - qr_i \cos(qr_i)}{(qr_i)^3} \right]^2 dr_i, \quad (\text{Equation 1})$$

$$\text{where } q = \frac{4\pi \sin \theta}{\lambda} \quad (\text{Equation 2})$$

ΔI is the intensity difference, q is the momentum transfer, which can be expressed as a function of scattering angle θ and wavelength of the incident beam λ , $scale$ is the scale factor, which is proportional to the volume fraction of the scatterer, $\Delta\rho$ is the difference in the SLDs of the scattering object and its surrounding, V is the volume of the scatterer ($4\pi r^3/3$), r is the radius of the scatterer, and f is the probability of size r for a log-normal distribution of r , which is a function of r , median of r , r_{med} , and the polydispersity, σ .

$$f(r, r_{med}, \sigma) = \frac{1}{Nr\sigma} e^{-0.5 \left(\frac{\ln(r) - \ln(r_{med})}{\sigma} \right)^2} \quad (\text{Equation 3})$$

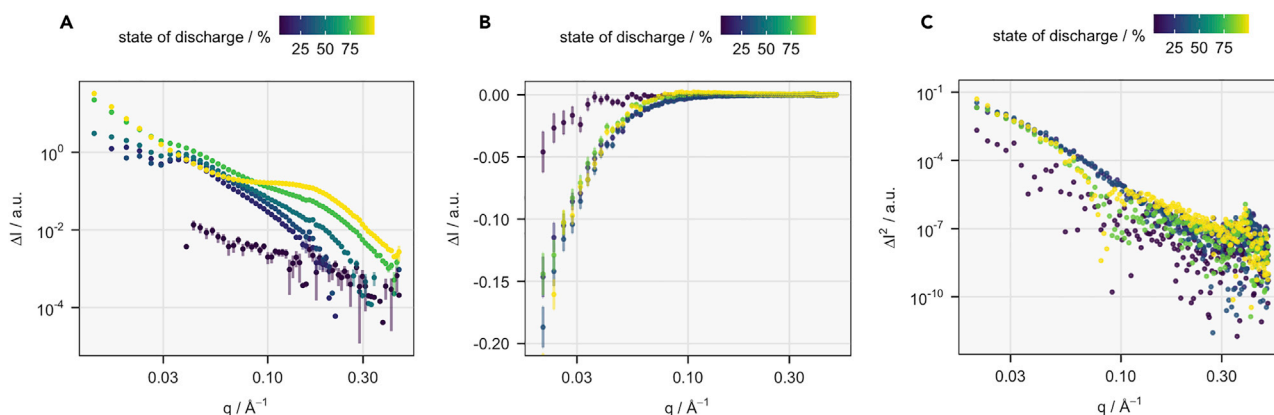


Figure 2. The intensity difference between selected measurements and the first measurement

The intensity difference, ΔI , between the data from selected states of discharge in the first cycle and the first measurement in the cells (A) SANS-D and (B) SAXS is plotted against the momentum transfer, q . The square of the intensity difference in (B) is plotted in (C). Note that the intensity axis has logarithmic scales in (A) and (C) but has a linear scale in (B). The error bars represent the uncertainty stemming from the measurements. A plot on expanded scales of the data in (B) is found in [Figure S4](#).

$$\text{with } N = \int_0^\infty Nf(r, r_{\text{med}}, \sigma) dr = 1 \quad (\text{Equation 4})$$

N is a normalization factor, which is calculated after the other parameters are chosen. The model was used to sequentially fit the data from the lower potential plateaus in the q range between 0.03 and 0.3 \AA^{-1} in the batch mode with chain-fitting using the Differential Evolution Adaptive Metropolis (DREAM) algorithm. A lower limit of the radius of one of the spheres was set to be 30 \AA when fitting the SANS data. Since the SLD of the electrolyte may be varied by its composition, $\Delta\rho$ is set to 1 in the fitting. Thus, the scale shown in the data is proportional to the product of the square of the difference in the contrast and the volume fraction of the scatterers ($\Delta\rho^2 \times \text{scale}$). The appropriateness of the two-sphere model is validated by the lack of correlation between the fitting parameters, as shown in [Figure S5](#).

The parameters extracted from fitting the scattering data of the SANS-D and SAXS cells are shown in [Figures 3 and 4](#), respectively. The analysis is focused on the lower voltage plateaus because there are no significant features in the scattering curves at the fully charged state, which can be observed in [Figure 1B](#). As displayed in [Figure S6](#), diffractions of β -S from the SAXS cell are detected by the WAXS detector, but the discontinuous spots, instead of a continuous Debye-Scherrer ring, suggest that the crystallites are large and thus outside the pores of the carbon matrix, as reported previously.^{32,33}

Since the cells were cycled at several C-rates, it is easier to start the comparison from the second cycle of the SANS-D cell and the third, fourth, and fifth cycles of the SAXS cell, all of which are at C/10. Although the second cycle of the SAXS cell is also at C/10, its features on the SAXS data are different from those from the subsequent cycles, especially for the parameters of the larger sphere. In [Figure 3](#), the scale factor of the smaller sphere (green squares) starts to increase shortly after the lower discharge plateau begins while its radius stays rather constant until the end of discharge. As mentioned in the [experimental procedures](#), it is important to note that the scale factor here is proportional to the product of the scatterer concentration and the square of the SLD contrast. If this smaller sphere models the formation of Li_2S particles in the electrolyte as we suggest,

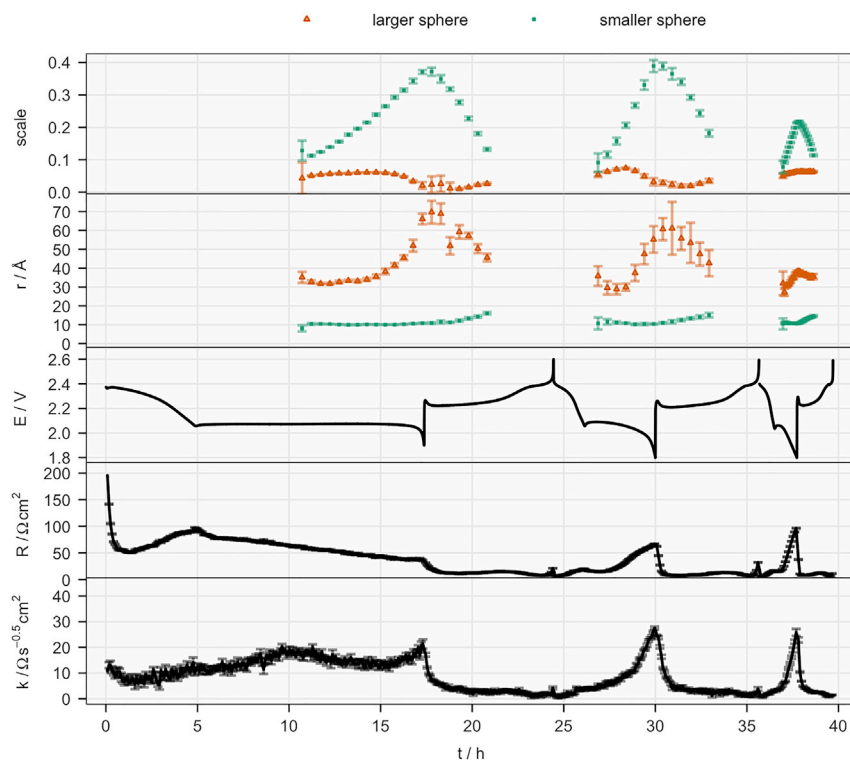


Figure 3. Results from the operando SANS measurements of the SANS-D cell

From top to bottom, the scale factor, $scale$; radius, r ; potential, E ; internal resistance, R ; and diffusion resistance coefficient, k , of the positive electrode are plotted against experimental time, t . A two-sphere model is applied to fit the intensity difference, ΔI , between the SANS data for each time interval and the first measurement. The parameters of the larger and smaller sphere distributions are plotted in orange triangles and green squares, respectively. The scale factor here is the product of a term that would correspond to the number density of the objects that give rise to scattering and the square of the difference in scattering length density, $\Delta\rho$.² The first discharge and charge are at C/20 and C/10, respectively. The second and third cycles are at C/10 and C/5, respectively. The error bars of the scale and radius represent their standard deviations from model fitting while those of the internal resistance and diffusion resistance coefficient represent the standard deviations resulted from the linear regression applied in the ICI method.

the contrast will not change significantly, which is also seen in Figure 2A. Therefore, the scale factor of the smaller sphere reflects mostly the number of particles, which is also the case for the SAXS results according to Figure 2B. The information from the different contrasts thus clarifies the composition of the observed particles at different times. This linear increase is also confirmed by the integrated intensity of the 111 reflection from Li_2S recorded by the WAXS detector in Figure 4. It is interesting that the radius derived from the SAXS results is smaller than that calculated from the WAXS data using the Scherrer equation, as shown in Figure S7. A similar discrepancy between these two methods of determining the particle size has been reported before with precisely controlled samples.³⁴ This can arise from polydispersity that is not readily included in the analysis of the peak width of diffraction peaks.

In some cycles of the SAXS cell, the first measurement that renders an acceptable fit appears later than that apparent in the SANS data and the first detection of Li_2S by WAXS. This is a consequence of the lower contrast between the Li_2S and the electrolyte compared with the contrast between the electrolyte and carbon, which

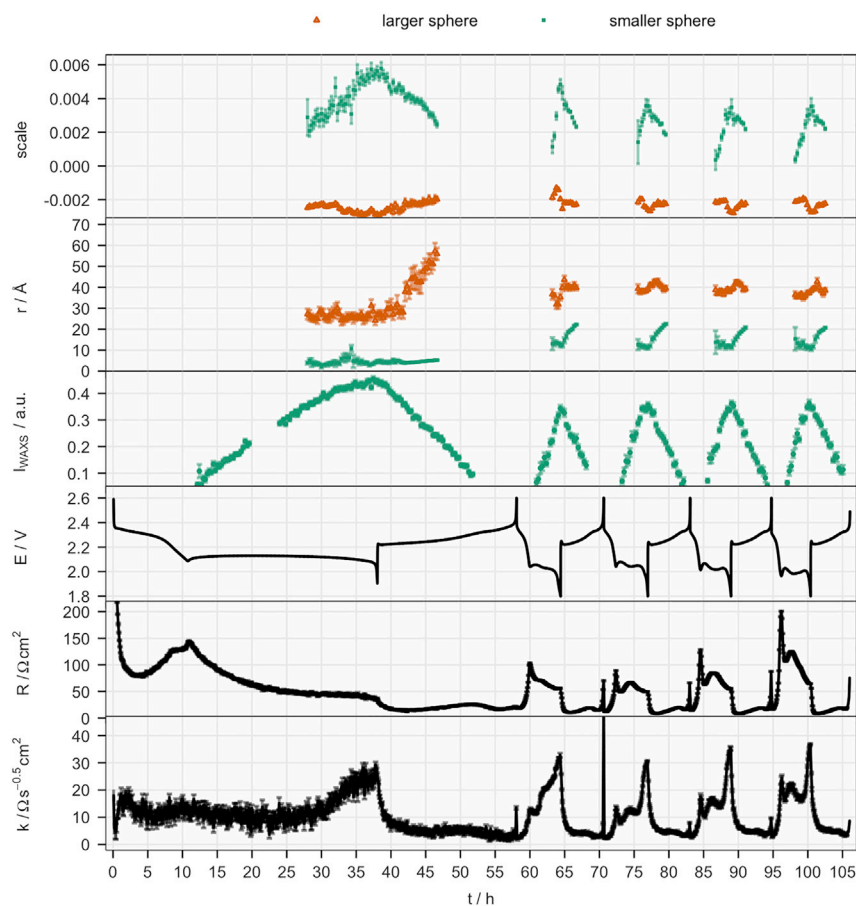


Figure 4. Results from the operando SAXS measurements

From top to bottom, the scale factor, scale ; radius, r ; the integrated intensity from the 111 diffraction peak of Li_2S , I_{WAXS} ; the potential, E ; internal resistance, R ; and diffusion resistance coefficient, k , of the positive electrode are plotted against experimental time, t . A two-sphere model is applied to fit intensity differences, ΔI , between the SAXS data in each interval and the first measurement. The parameters for the larger and smaller sphere distributions are plotted in orange triangles and green squares, respectively. The scale factor here is the product of a number concentration of scattering objects and the square of the difference in scattering length density, $\Delta\rho$.² The first discharge and charge are at C/50 and C/25, respectively. The subsequent cycles are at C/10. The SAXS and WAXS measurements were paused from the 20th to the 24th hours. The error bars of the scale, radius, and integrated intensity represent their standard deviations from model fitting while those of the internal resistance and diffusion resistance coefficient represent the standard deviations resulted from the linear regression applied in the ICI method.

contributes negatively to the intensity difference and may cancel out the positive signal from the precipitation. Nevertheless, during discharge, a linear increase in the scale factor of the smaller sphere is also present in the SAXS data. As the cells start to be charged, a linear decrease in the scale factor of the smaller sphere and the intensity from WAXS can be observed. Interestingly, the radius of the smaller sphere increases on charging, which indicates that the small clusters or particles of Li_2S disappear first, leaving a population with lower concentration and larger radius. This trend in Li_2S dissolution was reported in a previous SANS work.²⁸

The negative scale factor for the larger spheres (orange triangles) in Figure 4 results from the negative ΔI in the smaller q range in Figure 2B. The decrease in intensity cannot describe a formation process according to Equation 1. Given the contrast

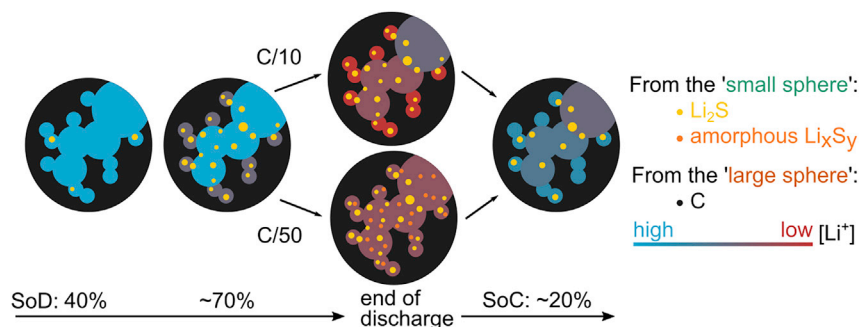


Figure 5. Scheme that summarizes the discharge and charge processes during the lower voltage plateau in the positive electrode of a Li-S cell

The approximate states of discharge (SoD) and charge (SoC) are shown at the bottom. The color of the electrolyte inside the pores of the carbon indicates the Li^+ concentration, which starts to drop inside the small pores. At a medium C-rate, C/10, the discharge process is stopped by the deficiency of Li^+ inside the mesopores, whereas, at a low C-rate, C/50, less Li^+ -demanding Li_xS_y forms and more discharge capacity can be delivered.

of the cell components in Figure 2B, it is reasonable to assign this spherical model to the change in the scattering intensity from the electrolyte inside the porous carbon. This interpretation is consistent with the positive scale factor of the larger sphere in Figure 3 since the contrast for neutrons between the deuterated electrolyte and carbon increases as discharge occurs, as shown in Table 2 and Figure S3. In the first two cycles in Figure 3, as the scale factor of the larger sphere remains roughly constant, the scale factor of the smaller sphere instead starts to increase. However, at the end of discharge, the larger sphere's scale factor drops as its radius increases. This phenomenon may be explained by the decreased ratio between Li and S atoms in the electrolyte inside the carbon matrix at the end of discharge. Suppose the pore structure of the carbon matrix does not change, the variation of the scale factor of the larger sphere in Figures 3 and 6 indicates that the SLD of the electrolyte increases for both neutrons and X-rays, as sketched in Figure S3. In the case of neutrons, this increase can be qualitatively reasoned by the removal of Li_2S_6 since it decreases when Li_2S_6 is added to the electrolyte. However, the same reasoning cannot be applied to the X-ray SLD since it increases when Li_2S_6 is added. Since, for X-rays, sulfur and lithium have a higher and lower electron density than the electrolyte, respectively, the increase for the electrolyte at the end of discharge suggests that the ratio of the removed lithium and sulfur should be much higher than 1:3 in Li_2S_6 . Given the large amount of lithium required to form Li_2S , it can be inferred that there is a deficiency of Li^+ in the mesopores of the carbon matrix, which has been reported in experiments³⁵ and simulations.³⁶

The increase in the radius of the larger sphere suggests that the resulting decrease in the contrast of SLD, as illustrated by the dashed lines in Figure 2, starts from the smaller pores, where a higher density of electrochemical reaction takes place due to the high specific conductive surface area. The data recorded during the third and fourth cycles of the SAXS measurements displayed in Figure 4 corroborate this explanation. Despite the smaller degree of variation, the radius of the larger spheres increases, and the scale factor decreases at the end of discharge. The more subtle change of the larger sphere in the SAXS data can be attributed to the smaller expected variation in the contrast of the electrolyte. While both Li and S have a smaller neutron SLD than the deuterated electrolyte, for X-rays, these are, respectively, below and above that of the pure electrolyte. Thus, the effect of the

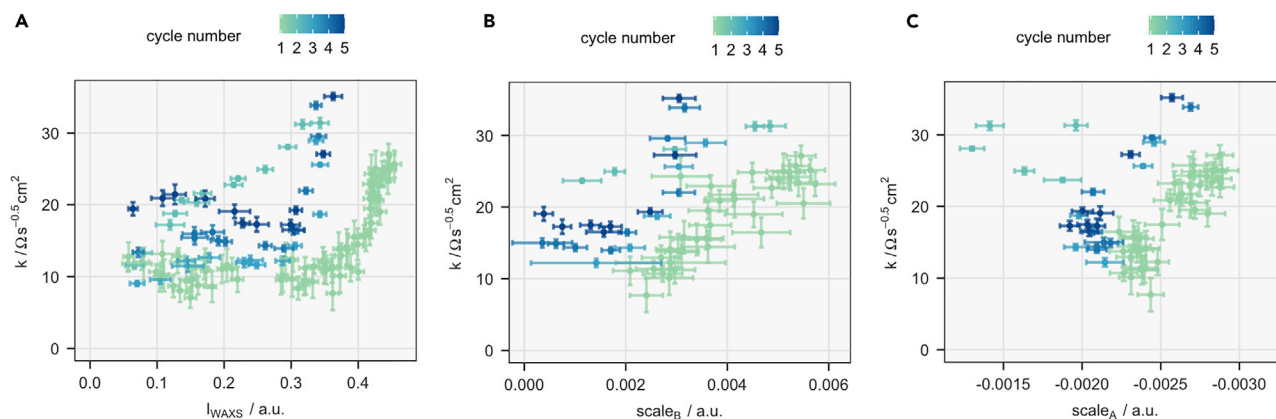


Figure 6. Correlation between the diffusion resistance coefficient and parameters derived from fitting the SAXS data

The diffusion resistance coefficient (k) plotted against (A) intensity of the 111 reflection of Li_2S (I_{WAXS}), (B) the scale factor for the smaller sphere, scale_B , and (C) the scale factor for the larger spheres, scale_A , from the fitting results for the SAXS data shown in Figure 4. Note that the x axis is reversed in (C). The error bars of the scales and intensity represent their standard deviation from model fitting while those of the diffusion resistance coefficient represent the standard deviation resulted from the linear regression applied in the ICI method.

removal of both Li and S from the electrolyte can be expected to be more obvious in SANS with the deuterated electrolyte than in SAXS.

As the charging starts in the first two cycles in Figure 3, the radius of the larger spheres decreases, while its scale factor remains low for a longer time before increasing again. This is consistent with the outward migration of Li^+ from the positive electrode, which starts from the large pores of the carbon matrix if a hierarchical pore structure is assumed. Thus, the contrast between the electrolyte and carbon decreases in the large pores at the beginning of the charging and gives rise to the decrease in the radius of the larger sphere in the fitted results. Subsequently, Li^+ may be replenished by the dissolution of Li_2S located in the small pores to sustain the outward flow. Nonetheless, the fitting results for these larger scattering objects during charging have less certainty due to the small values of the scale factors.

Influence of the specific current (C-rate) on the precipitation of Li_2S

Based on the scattering data, the precipitation behaviors can be categorized into three groups, which are present at high (C/5), medium (C/10 and C/20), or low (C/50) C-rates.

As discussed earlier, when the cell is discharged at medium C-rates, the scale factor of the smaller sphere in Figures 3 and 6 indicates that the concentration of Li_2S increases linearly, which is also observed by WAXS. The radius of the precipitates remains around 10 Å throughout the discharge process. The lack of variation in the scattering from the SANS-H cell suggests that the formation of Li_2S is unlikely to expand the pores of the carbon matrix. Therefore, it is reasonable to conclude that most of the Li_2S precipitates are in the mesopores (2–50 nm) since their size is comparable with that of the micropores. Although this suggests that a direct pore blockage of one single particle is unlikely, the large number of small Li_2S particles can compromise the transport properties inside the carbon matrix by replacing the volume of ionic conducting electrolyte. This is manifested by both the Li^+ depletion shown by the larger sphere, as discussed earlier, and the sharp increase in the diffusion resistance coefficient in Figure 3. Eventually, the deficiency of Li^+ inside the carbon matrix leads to the termination of discharge at a medium C-rate.

At C/50, the low C-rate, the radius of the precipitates is only around 5 Å, as shown in the first cycle in Figure 4. This reduction in particle size is contrary to the trend observed with WAXS in Figure S7 and in previous SEM and X-ray imaging reports.^{18,22} This discrepancy in the observed particle size indicates that a large portion of the precipitates may be amorphous small particles in the electrolyte that cannot be detected by XRD and imaging and are washed away with the electrolyte during *ex situ* sample preparation. Both the scale factor from SAXS and the peak intensity from WAXS reach higher values by the end of discharge compared with the subsequent cycles at C/10. While the former increases linearly throughout the discharge, the latter slows down after $t = 30$ h. This suggests that the precipitates forming at the last stage are amorphous. This observation provides evidence for the formation of amorphous species, e.g., Li_2S_2 , which is also proposed by the previous XRD study¹⁶ based on the mismatch between the amount of Li_2S and discharge capacity. The formation of less Li-demanding Li_xS_y ($y/x > 0.5$) following the precipitation of Li_2S may be one of the reasons why higher sulfur utilization can be achieved at the low C-rate, while this secondary reaction may not be able to sustain a higher current.

At the high C-rate, C/5, the size of the precipitates is similar to that at medium or slow C-rates, but the scale factor only reaches half of that under lower currents, as depicted in Figure 3. The scale factor for the larger spheres remains constant during the discharge process, indicating that there is no significant decrease in Li^+ concentration as in the cases with medium currents. Since there are no other obvious features from the SANS results, the limiting factor of the discharge process may not be detected by that technique. Given the higher internal resistance at the end of discharge compared with the previous cycle at C/10, a probable cause might include the higher solution resistance in the electrolyte, resulting from the different polysulfide species at different currents.

Based on the above discussions about the results from Figures 3 and 4, the discharge and subsequent charge processes at medium, C/10, and low, C/50, C-rates are summarized by the scheme in Figure 5. The trends in the Li^+ concentration are derived from the scale factor and radius of the larger sphere. As discussed at the end of section “cell modification and assembly,” the increase in radius at C/10 indicates that Li^+ is more depleted in the smaller pores than in the bigger ones, while at C/50, the radius remains constant, indicating that the Li^+ concentration is uniformly low in the pores of the carbon matrix. In addition, from the comparison between SAXS and WAXS results in Figure 4, it can be concluded that in addition to the precipitation of Li_2S , which is already more than at C/10, an amorphous discharge product forms at the last stage of discharge at C/50.

Influence of the precipitation on the electrochemical properties

To take a closer look at the effect of precipitation, in Figure 6, the diffusion resistance coefficient is plotted against the scale factors and diffraction intensity from Figure 4. The SAXS data are chosen as they were measured over more cycles, and the employed electrolyte is more widely used in the field. Despite the similar chemical properties, tetrahydrofuran does not behave in the same way as 1,3-dioxolane when serving as a co-solvent in Li-S cells, as demonstrated in Figures S8 and S9.

In Figure 6, a consistent trend can be observed in the data for cycles 3–5. The sharp increase in the diffusion resistance coefficient as the WAXS intensity reaches 0.3 agrees with a previous *operando* diffraction study.¹⁹ Since the coefficient reflects both the transport properties inside a porous electrode¹⁹ and diffusion processes

coupled with an electrochemical reaction,³⁷ the previous study assigned its rapid increase at the end of discharge to the worsened transport properties inside the carbon matrix due to the replacement of the electrolyte volume by the Li_2S particles. Although a hyperbolic increase in k is expected with a linear increase in the volume fraction of Li_2S , as shown in the previous work,¹⁹ a linear correlation between k and the scale factor of the larger sphere (scale_A) in cycles 1, 3, 4, and 5 can also be observed here in Figure 6C. As explained in section “cell modification and assembly,” the decrease in the scale factor of the larger sphere may indicate a drop in Li^+ concentration in the mesopores of the carbon matrix, which leads to an increase in the diffusion resistance.

For cycle 1, the scale factors of both larger and smaller spheres show a linear correlation with the diffusion resistance coefficient. As discussed in the previous section, the formation of amorphous particles dominates at the last stage of this slow discharge at C/50. The correlation in Figure 6B shows that the later formed amorphous particles contribute to the diffusion resistance, together with the drop in Li^+ concentration indicated by Figure 6C.

The electrochemical data from the second cycle are the outlier of the four cycles at C/10. The more consistent behavior after the third cycle has been observed in previous studies. In Figure 6, linear correlations can be found between k and both WAXS intensity and the intensity scale factor for the smaller spheres but not between k and the scale factor of the larger pores in the second cycle. This suggests that the diffusion resistance in the second cycle is mostly influenced by the worse transport properties caused by Li_2S particles. The distinct behavior of the second cycle may be speculated to stem from the relaxation of the electrode structure and/or redistribution of the active materials, which is subsequently stabilized.

Conclusions

This work has characterized the precipitation and dissolution processes in Li-S batteries during the lower discharge and charge voltage plateaus by small-angle scattering in three contrasts, SANS with both hydrogenous and deuterated electrolytes and SAXS. Both SANS and SAXS data can be fitted to the same model of two sizes of spheres. The evolution of the smaller spheres corresponds well with the intensity of Li_2S crystals observed in the WAXS measurements, while the larger spheres can be attributed to varying composition of the catholyte in the mesopores of the carbon matrix. Analysis indicates that the precipitates are small and unlikely to block the pores of the carbon matrix. At C/10 and C/20, the end of discharge shows a strong correlation with the change in the contrast of the larger spheres, which may be attributed to Li^+ deficiency in the electrolyte in the mesopores of the carbon matrix. This is corroborated by the correlation between the scale factor of the larger sphere and the simultaneously measured diffusion resistance. These findings imply that the supply of Li^+ in the carbon matrix is the limiting factor for sulfur utilization of a mesoporous sulfur/carbon composite electrode with high specific surface area. The passivation of the carbon matrix or polysulfide diffusion may play more minor roles in this context, but the case can certainly differ for different types of carbon hosts.

EXPERIMENTAL PROCEDURES

Resource availability

Lead contact

Further information and requests for resources should be directed to and will be fulfilled by the lead contact, Daniel Brandell (daniel.brandell@kemi.uu.se).

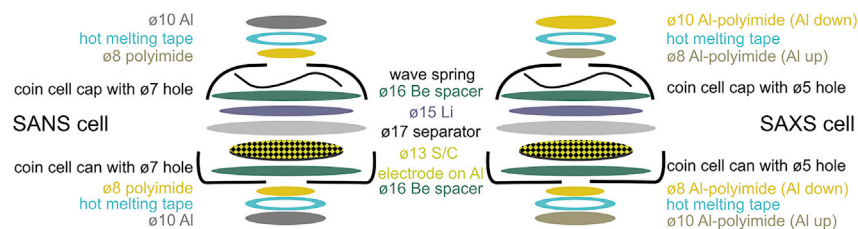


Figure 7. Schematic illustration of the modified coin cells for operando SANS and SAXS experiments

The diameters shown with the symbol \varnothing are in millimeters.

Materials availability

This study did not generate new materials.

Data and code availability

The raw data, processed data, and analysis scripts written in the R programming language are available at Zenodo: <https://doi.org/10.5281/zenodo.5526828>.³⁸

The raw data for the SANS measurements conducted at Institut Laue-Langevin are available on their own data deposit (<https://doi.org/10.5291/ILL-DATA.1-04-200>).³⁹

Materials

Elemental sulfur powder (S, Sigma-Aldrich), Ketjenblack (EC-600JD, Akzo Nobel), Super C65 (Imerys), carbon nanofibers (CNFs, 20–200 nm in cross-sectional diameter and 100 μm in length, Sigma-Aldrich), poly(ethylene oxide) (PEO, $M_w \sim 4\,000\,000$, Sigma-Aldrich), poly(vinylpyrrolidone) (PVP, $M_w \sim 360\,000$, Sigma-Aldrich), C-coated Al foil (20 μm thick, SDX, Showa Denko), beryllium discs (99+%, $\varnothing 16$ mm, 0.25 mm thick, American Elements), Al-coated polyimide (25 μm thick coated with 30 nm Al on one side, Goodfellow), Al foil (20 μm thick, Korff AG), polyimide film (25 μm thick, Goodfellow), coin cells (CR2025, Hohsen), and hot-melting tape (thermo bonding film, Maskin & Verktyg, Sweden) were used as received. Lithium metal foil (Li, 125 μm thick, Cyprus Foote Mineral) was also used as received but stored under an Ar atmosphere. Lithium bis(trifluoromethanesulfonyl)imide (LiTFSI, BASF) and lithium nitrate (LiNO_3 , Sigma-Aldrich) were dried at 120°C under vacuum for 12 h. 1,2-dimethoxyethane (DME, BASF), 1,3-dioxolane (DOL, Sigma-Aldrich), tetrahydrofuran (THF, Sigma-Aldrich), 1,2-dimethoxyethane- D_{10} (d-DME, 99.5 at% D, Sigma-Aldrich), and tetrahydrofuran- D_8 (d-THF, ≥ 99.5 at% D, Sigma-Aldrich) were dried with 3 Å molecular sieves for at least 12 h. Celgard® 2400 separators were dried under vacuum at 80°C for 8 h.

Cell modification and assembly

Schematic illustrations of the modified CR2025 coin cells for operando SANS and SAXS measurements are shown in Figure 7. The electrode stack was sandwiched by two Be spacers to ensure uniform stack pressure and conductivity in both cells. For SAXS, the windows (5 mm in diameter) were optimized for X-ray transmission; so, the minimal amounts of Al and polyimide were used to attain sufficient sealing. For SANS, the windows (7 mm in diameter) were optimized for sealing since transmission of these materials was not a major concern and the cells had to be transported to the beamline. The scattering curves of the various individual cell components that the beam passes through are shown in Figure S1.

The S/C composite electrodes in all the cells were fabricated according to a previously optimized procedure.³⁰ A slurry with 65% S, 21% Ketjenblack, 3.5% C65,

3.5% CNF, 5.6% PEO, and 1.6% PVP (by mass) was prepared with 20 vol % isopropanol solution in deionized water. Sulfur and Ketjenblack were mixed in a mortar and heated to 155°C for 20 min before mixing with other ingredients for 2 h in a planetary ball mill. The slurry was coated with a doctor blade onto the C-coated Al foil before being dried in the atmosphere and cut into \varnothing 13 mm discs. The electrodes were dried in vacuum at 55°C for 12 h before use.

The modified and conventional coin cells were assembled in the same way. The electrode stack consisted of a S/C composite electrode, Celgard 2400 (\varnothing 17 mm), and Li (\varnothing 15 mm), which was a half-cell configuration due to the excess capacity of Li. The electrolyte was composed of 1 molal LiTFSI and 0.25 molal LiNO₃ in different solvents for different cells, which are listed with the electrolyte-to-sulfur (e/S) ratios in Table 1. Conventional coin cells were made with DME:DOL and DME:THF for benchmarking the electrochemical properties of the modified coin cells, as shown in Figures S8 and S9. It can be observed that the modified coin cells exhibit specific capacity comparable with that of the conventional coin cells. However, the modified coin cells show higher resistance, which grows with the number of cycles and can thus be attributed to the loss of electrolyte due to imperfect sealing of the windows. Nevertheless, the features of the potential and resistance profiles are representative of those of conventional coin cells.

Operando SANS

The SANS experiments were made with the D33 instrument at the Institut Laue-Langevin (ILL), France.⁴⁰ The wavelength of neutron was set to 6 Å. Around 48 h after the cell assembly and transport, the two cells, SANS-D and SANS-H, were measured alternately for 900 s while they were discharged to 1.9 V at a constant C-rate of C/25 (where 1C is defined as 1,672 mA g_s⁻¹, and g_s denotes the mass of sulfur in grams), charged to 2.6 V at C/10, cycled between 1.8 and 2.6 V at C/10, and finally cycled between 1.8 and 2.6 V at C/5 by a SP-240 and a SP-150 potentiostat (Bio-Logic), respectively. The cells were mounted on a custom-built sample holder with electrical connections, which is fixed onto the sample stage at the beamline, as displayed in Figure S9. The cells were then linearly translated back and forth in the direction perpendicular to the neutron beam automatically by the sample stage. As the SANS-H cell had finished the planned program, the alternation stopped, and all the following measurements were done on the SANS-D cell. Transmissions of both cells were measured before and after the *operando* measurements. The transmission of the SANS-D cell changed from 0.86788 to 0.86252, while that of the SANS-H cell changed from 0.80680 to 0.81073. Both changes are less than 0.75%.

During the galvanostatic cycling, the current was paused for 1 s every 5 min. While the current was off, the voltage was measured every 0.1 s and analyzed by the previously reported ICI method, as described below in section “*operando* SAXS and WAXS.”

Operando SAXS and WAXS

The SAXS and WAXS measurements were conducted with a Xeuss 2.0 SAXS/WAXS system (Xenocs) with a Cu K α X-ray source (λ = 1.54 Å) and a Pilatus 300 k detector at 270 mm from the sample. The wide-angle detector, Pilatus 100k, was at 161 mm from the sample and provided further diffraction data to a scattering angle of about 40°. After the cell assembly and a 6 h rest, the SAXS cell was discharged to 1.9 V at C/50, charged to 2.6 V at C/25, and subsequently cycled between 1.8 and 2.6 V at C/10. As with SANS measurements, a SP-150 potentiostat (Bio-Logic) was used for the control of discharge and charge and the measurement

of electrical properties. Each measurement was collected in vacuum for 890 s and normalized to the transmission, recorded on the detector that was operated with no beam stop. The transmission of the measurements included in the fitting is shown in [Figure S11](#). The same protocol of the ICI method was applied and it was revealed that the internal resistance of the cell increases substantially after the sixth cycle. Therefore, the analysis of the cell was focused on the first five cycles.

Interpretation of scattering data

The azimuthal averages of the two-dimensional raw data from the SANS and SAXS measurements were made with GRASP⁴¹ and Foxtrot⁴² software, respectively. The overall scattering from the cells, as seen in [Figure 1](#), is intense and has a complex shape. Scattering can be attributed to various components that include electrodes, seals, separator, and window materials, as well as electrolyte in the bulk and within pores. Although data are normalized to direct beam intensity and corrected to allow for the overall transmission, the uncertainty in the thickness of the various parts of the cell precludes simple presentation in usual absolute units of scattering cross section. The focus is made directly on the changes in scattering and how these differ for the contrasts available to neutrons and X-rays for the various relevant electrochemical processes.

To fit the data from the SANS-D and SAXS cells, the first measurement was subtracted from the subsequent measurements to exclude the background from unchanging components and to highlight the differences. With the plug-in model function in the SasView software,⁴³ the two-sphere model, described by Equations 1, 2, 3 and 4, was built by adding two sphere models with polydispersity. The rest of the data analysis is explained previously in section “[application and interpretation of the two-sphere model](#).”

The WAXS data were analyzed by modeling the 111 reflection of Li_2S ($Fm\bar{3}m$) using Topas Academic (V6) software. The reflection was modeled using a single Gaussian peak with the intensity and width refined and the position constrained to the angular range of $24.5\text{--}27.5^\circ$ (2θ). A fourth-degree Chebychev polynomial was used to model the background.

Analysis of the electrochemical data

Following the ICI method, a linear regression of potential change (ΔE) against the square root of step time ($t^{0.5}$) was performed to the data collected during each current interruption. The internal resistance, R , was obtained by dividing the intercept ($\Delta E(t = 0)$) by the current before the current pause, and the diffusion resistance coefficient (k) was determined by dividing the gradient, $dE/d\sqrt{t}$, by the current before the interruption. Based on the porous electrode model,⁴⁴ it has been demonstrated that R is the sum of the electronic, solution, and charge-transfer resistances, and k is a measure of the time-dependent resistance, which is a direct current analogy to the Warburg element used in equivalent circuit models for analyzing electrochemical impedance spectroscopy.^{19,31} Under an alternating current perturbation, the impedance of a Warburg element, Z_W , can be expressed as follows:⁴⁵

$$Z_W = (1 - j)W\omega^{-0.5}, \quad (\text{Equation 5})$$

where j is the imaginary number, W is the Warburg coefficient, and ω is the angular frequency. In previous work, it was theoretically derived that k is proportional to W , and the linear relationship was experimentally verified over a wide range of states of charge in the Li-S system.¹⁹

$$k = \sqrt{\frac{8}{\pi}} \cdot W \quad (\text{Equation 6})$$

A script in the R programming language⁴⁶ was written for the ICI analysis, which can be found with the raw data via Zenodo.³⁸

SUPPLEMENTAL INFORMATION

Supplemental information can be found online at <https://doi.org/10.1016/j.chempr.2022.03.001>.

ACKNOWLEDGMENTS

The authors are grateful to ILL for the access to the D33 beamline granted for the experiment no. 1-04-200. The authors also thank the STandUP for energy consortium. This work benefited from the use of the SasView application, originally developed under NSF award DMR-0520547. SasView contains code developed with funding from the European Union's Horizon 2020 research and innovation program under the SINE2020 project, grant 654000.

AUTHOR CONTRIBUTIONS

Conceptualization, Y.-C.C., M.J.L., D.B., and A.R.R.; methodology, Y.-C.C. and A.R.R.; investigation, Y.-C.C., N.-J.S., and A.R.R.; writing – original draft, Y.-C.C. and A.R.R.; writing – review and editing, Y.-C.C., M.J.L., D.B., and A.R.R.; visualization, Y.-C.C.; supervision, M.J.L., D.B., and A.R.R.; funding acquisition, D.B.

DECLARATION OF INTERESTS

The authors declare no competing interests.

Received: October 5, 2021

Revised: November 5, 2021

Accepted: February 28, 2022

Published: March 22, 2022

REFERENCES

1. Wujcik, K.H., Wang, D.R., Teran, A.A., Nasybulin, E., Pascal, T.A., Prendergast, D., and Balsara, N.P. (2018). Determination of redox reaction mechanisms in lithium-sulfur batteries. *Electrochem. (John Wiley & Sons, Ltd)*, 41–74. <https://doi.org/10.1002/9783527807215.ch3>.
2. Bonnick, P., and Muldoon, J. (2020). The Dr Jekyll and Mr Hyde of lithium sulfur batteries. *Energy Environ. Sci.* 13, 4808–4833. <https://doi.org/10.1039/D0EE02797A>.
3. Ye, G., Zhao, M., Hou, L.P., Chen, W.-J., Zhang, X.Q., Li, B.Q., and Huang, J.Q. (2022). Evaluation on a 400 Wh kg⁻¹ lithium-sulfur pouch cell. *J. Energy Chem.* 66, 24–29. <https://doi.org/10.1016/j.jechem.2021.07.010>.
4. Shateri, N., Auger, D.J., Fotouhi, A., and Brighton, J. (2021). An experimental study on prototype lithium-sulfur cells for aging analysis and state-of-health estimation. *IEEE Trans. Transp. Electrification*, 7, 1324–1338. <https://doi.org/10.1109/TTE.2021.3059738>.
5. Shi, L., Bak, S.-M., Shadike, Z., Wang, C., Niu, C., Northrup, P., Lee, H., Baranovskiy, A.Y., Anderson, C.S., Qin, J., et al. (2020). Reaction heterogeneity in practical high-energy lithium-sulfur pouch cells. *Energy Environ. Sci.* 13, 3620–3632. <https://doi.org/10.1039/D0EE02088E>.
6. Mikhaylik, Y.V., and Akridge, J.R. (2004). Polysulfide shuttle study in the Li/S battery system. *J. Electrochem. Soc.* 151, A1969. <https://doi.org/10.1149/1.1806394>.
7. Wild, M., O'Neill, L., Zhang, T., Purkayastha, R., Minton, G., Marinescu, M., and Offer, G.J. (2015). Lithium sulfur batteries, a mechanistic review. *Energy Environ. Sci.* 8, 3477–3494. <https://doi.org/10.1039/C5EE01388G>.
8. Scheers, J., Fantini, S., and Johansson, P. (2014). A review of electrolytes for lithium-sulphur batteries. *J. Power Sources* 255, 204–218. <https://doi.org/10.1016/j.jpowsour.2014.01.023>.
9. Zech, C., Hönicke, P., Kayser, Y., Risse, S., Grätz, O., Stamm, M., and Beckhoff, B. (2021). Polysulfide driven degradation in lithium-sulfur batteries during cycling - quantitative and high time-resolution operando X-ray absorption study for dissolved polysulfides probed at both electrode sides. *J. Mater. Chem. A* 9, 10231–10239. <https://doi.org/10.1039/D0TA12011A>.
10. Bombelli, P., Müller, T., Herling, T.W., Howe, C.J., and Knowles, T.P. (2015). Structural design of cathodes for Li-S batteries. *Adv. Energy Mater.* 5, 1–6. <https://doi.org/10.1002/aenm.201401299>.
11. Risse, S., Juhl, A., Mascotto, S., Arlt, T., Markötter, H., Hilger, A., Manke, I., and Fröba, M. (2020). Detailed and direct observation of sulfur crystal evolution during operando analysis of a Li-S cell with synchrotron imaging. *J. Phys. Chem. Lett.* 11, 5674–5679. <https://doi.org/10.1021/acs.jpclett.0c01284>.
12. Harks, P.P.R.M.L., Robledo, C.B., Verhallen, T.W., Notten, P.H.L., and Mulder, F.M. (2017). The significance of elemental sulfur dissolution in liquid electrolyte lithium sulfur batteries. *Adv. Energy Mater.* 7, 1601635. <https://doi.org/10.1002/aenm.201601635>.
13. Shen, C., Andrei, P., and Zheng, J.P. (2019). Stable cycling of lithium-sulfur batteries by optimizing the cycle condition. *Electrochim. Acta* 326, 134948. <https://doi.org/10.1016/j.electacta.2019.134948>.

14. Lin, Y., Chen, D., Wang, S., Han, D., Xiao, M., and Meng, Y. (2020). Addressing passivation of a sulfur electrode in Li-S pouch cells for dramatically improving their cyclic stability. *ACS Appl. Mater. Interfaces* 12, 29296–29301. <https://doi.org/10.1021/acsami.0c05385>.
15. Drvarič Talian, S., Kapun, G., Moškon, J., Vizintin, A., Randon-Vitanova, A., Dominko, R., and Gaberšček, M. (2019). Which process limits the operation of a Li-S system? *Chem. Mater.* 31, 9012–9023. <https://doi.org/10.1021/acs.chemmater.9b03255>.
16. Walus, S., Barchasz, C., Bouchet, R., Leprêtre, J.-C., Colin, J.-F., Martin, J.-F., Elkaïm, E., Baehz, C., and Alloin, F. (2015). Lithium/sulfur batteries upon cycling: structural modifications and species quantification by in situ and operando X-ray diffraction spectroscopy. *Adv. Energy Mater.* 5, 1500165. <https://doi.org/10.1002/aenm.201500165>.
17. Zhang, T., Marinescu, M., Walus, S., Kovacic, P., and Offer, G.J. (2018). What limits the rate capability of Li-S batteries during discharge: charge transfer or mass transfer? *J. Electrochem. Soc.* 165, A6001–A6004. <https://doi.org/10.1149/2.0011801jes>.
18. Yu, S.H., Huang, X., Schwarz, K., Huang, R., Arias, T.A., Brock, J.D., and Abruña, H.D. (2018). Direct visualization of sulfur cathodes: new insights into Li-S batteries via operando X-ray based methods. *Energy Environ. Sci.* 11, 202–210. <https://doi.org/10.1039/C7EE02874A>.
19. Chien, Y.C., Menon, A.S., Brant, W.R., Brandell, D., and Lacey, M.J. (2020). Simultaneous monitoring of crystalline active materials and resistance evolution in lithium-sulfur batteries. *J. Am. Chem. Soc.* 142, 1449–1456. <https://doi.org/10.1021/jacs.9b11500>.
20. Lang, S.Y., Xiao, R.J., Gu, L., Guo, Y.G., Wen, R., and Wan, L.J. (2018). Interfacial mechanism in lithium-sulfur batteries: how salts mediate the structure evolution and dynamics. *J. Am. Chem. Soc.* 140, 8147–8155. <https://doi.org/10.1021/jacs.8b02057>.
21. Fan, F.Y., Carter, W.C., and Chiang, Y.M. (2015). Mechanism and kinetics of Li₂S precipitation in lithium-sulfur batteries. *Adv. Mater.* 27, 5203–5209. <https://doi.org/10.1002/adma.201501559>.
22. Kong, L., Chen, J.X., Peng, H.J., Huang, J.Q., Zhu, W., Jin, Q., Li, B.Q., Zhang, X.T., and Zhang, Q. (2019). Current-density dependence of Li₂S/Li₂S₂ growth in lithium-sulfur batteries. *Energy Environ. Sci.* 12, 2976–2982. <https://doi.org/10.1039/C9EE01257E>.
23. Sandi, G., Thiagarajan, P., Carrado, K.A., and Winans, R.E. (1999). Small angle neutron scattering characterization of the porous structure of carbons prepared using inorganic templates. *Chem. Mater.* 11, 235–240. <https://doi.org/10.1021/cm980333j>.
24. Härk, E., Petzold, A., Goerigk, G., Ballauff, M., Kent, B., Keiderling, U., Palm, R., Vaas, I., and Lust, E. (2019). The effect of a binder on porosity of the nanoporous RP-20 carbon. A combined study by small angle X-ray and neutron scattering. *Micropor. Mesopor. Mater.* 275, 139–146. <https://doi.org/10.1016/j.micromeso.2018.08.022>.
25. Smorgonskaya, É.A., Kyutt, R.N., Shuman, V.B., Danishevskii, A.M., Gordeev, S.K., and Grechinskaya, A.V. (2002). Small-angle x-ray scattering in a carbon-sulfur nanocomposite produced from bulk nanoporous carbon. *Phys. Solid State* 44, 2001–2008. <https://doi.org/10.1134/1.1514795>.
26. Petzold, A., Juhl, A., Scholz, J., Ufer, B., Goerigk, G., Fröba, M., Ballauff, M., and Mascotto, S. (2016). Distribution of sulfur in carbon/sulfur nanocomposites analyzed by small-angle X-ray scattering. *Langmuir* 32, 2780–2786. <https://doi.org/10.1021/acs.langmuir.5b04734>.
27. Zakharchenko, T.K., Avdeev, M.V., Sergeev, A.V., Chertovich, A.V., Ivankov, O.I., Petrenko, V.I., Shao-Horn, Y., Yashina, L.V., and Itkis, D.M. (2019). Small-angle neutron scattering studies of pore filling in carbon electrodes: mechanisms limiting lithium-air battery capacity. *Nanoscale* 11, 6838–6845. <https://doi.org/10.1039/C9NR00190E>.
28. Risse, S., Härk, E., Kent, B., and Ballauff, M. (2019). Operando analysis of a lithium/sulfur battery by small-angle neutron scattering. *ACS Nano* 13, 10233–10241. <https://doi.org/10.1021/acsnano.9b03453>.
29. Jafta, C.J., Prévost, S., He, L., Li, M., Sun, X.G., Yang, G., Belharouak, I., and Nanda, J. (2021). Quantifying the chemical, electrochemical heterogeneity and spatial distribution of (poly) sulfide species using operando SANS. *Energy Storage Mater.* 40, 219–228. <https://doi.org/10.1016/j.ensm.2021.05.016>.
30. Lacey, M.J., Österlund, V., Bergfelt, A., Jeschull, F., Bowden, T., and Brandell, D. (2017). A robust, water-based, functional binder framework for high-energy lithium-sulfur batteries. *ChemSusChem* 10, 2758–2766. <https://doi.org/10.1002/cssc.201700743>.
31. Lacey, M.J. (2017). Influence of the electrolyte on the internal resistance of lithium-sulfur batteries studied with an intermittent current interruption method. *ChemElectroChem* 4, 1997–2004. <https://doi.org/10.1002/celec.201700129>.
32. Risse, S., Jafta, C.J., Yang, Y., Kardjilov, N., Hilger, A., Manke, I., and Ballauff, M. (2016). Multidimensional operando analysis of macroscopic structure evolution in lithium sulfur cells by X-ray radiography. *Phys. Chem. Chem. Phys.* 18, 10630–10636. <https://doi.org/10.1039/c6cp01020b>.
33. Jafta, C.J., Hilger, A., Sun, X.G., Geng, L., Li, M., Risse, S., Belharouak, I., and Manke, I. (2020). A multidimensional operando study showing the importance of the electrode macrostructure in lithium sulfur batteries. *ACS Appl. Energy Mater.* 3, 6965–6976. <https://doi.org/10.1021/acsaem.0c01027>.
34. Jensen, H., Pedersen, J.H., Jørgensen, J.E., Pedersen, J.S., Joensen, K.D., Iversen, S.B., and Sogaard, E.G. (2006). Determination of size distributions in nanosized powders by TEM, XRD, and SAXS. *J. Exp. Nanosci.* 1, 355–373. <https://doi.org/10.1080/17458080600752482>.
35. See, K.A., Leskes, M., Griffin, J.M., Britto, S., Matthews, P.D., Emly, A., Van der Ven, A., Wright, D.S., Morris, A.J., Grey, C.P., and Seshadri, R. (2014). Ab initio structure search and in situ ⁷Li NMR studies of discharge products in the Li-S battery system. *J. Am. Chem. Soc.* 136, 16368–16377. <https://doi.org/10.1021/ja508982p>.
36. Thangavel, V., Xue, K.H., Mammeri, Y., Quiroga, M., Mastouri, A., Guéry, C., Johansson, P., Morcrette, M., and Franco, A.A. (2016). A microstructurally resolved model for Li-S batteries assessing the impact of the cathode design on the discharge performance. *J. Electrochem. Soc.* 163, A2817–A2829. <https://doi.org/10.1149/2.0051614jes>.
37. Chien, Y.C., Liu, H., Menon, A.S., Brant, W.R., Brandell, D., and Lacey, M.J. (2021). A fast alternative to the galvanostatic intermittent titration technique. *ChemRxiv*. <https://doi.org/10.26434/chemrxiv-2021-09srz>.
38. Chien, Y., Lacey, M.J., Brandell, D., Steinke, N.J., and Rennie, A.R. (2021). Supporting data for “correlations between precipitation reactions and electrochemical performance of lithium-sulfur batteries”. Zenodo. <https://doi.org/10.5281/zenodo.5526828>.
39. Brandell, D., Chien, Y.-C., Porcar, L., Rennie, A.R., and Steinke, N.J. (2021). Investigation of pore-blocking precipitation processes and their impact on the electrochemical properties in Li-S batteries. *Institut Laue-Langevin (ILL)*. <https://doi.org/10.5291/ILL-DATA.1-04-200>.
40. Dewhurst, C.D., Grillo, I., Honecker, D., Bonnaud, M., Jacques, M., Amrouni, C., Perillo-Marcone, A., Manzin, G., and Cubitt, R. (2016). The small-angle neutron scattering instrument D33 at the Institut Laue-Langevin. *J. Appl. Crystallogr.* 49, 1–14. <https://doi.org/10.1107/S1600576715021792>.
41. Dewhurst, C. GRASP. <https://www.ill.eu/users/support-labs-infrastructure/software-scientific-tools/grasp>.
42. Girardot, R., Viguier, G., Pérez, J., and Ounsy, M. (2015). FOXTROT: a JAVA-based application to reduce and analyze SAXS and WAXS piles of 2D data at synchrotron SOLEIL. *In Proceedings of the 8th canSAS Meeting, Tokai, Japan*, pp. 14–16.
43. SasView. <https://www.sasview.org/>.
44. de Levie, R. (1963). On porous electrodes in electrolyte solutions. *Electrochim. Acta* 8, 751–780. [https://doi.org/10.1016/0013-4686\(63\)80042-0](https://doi.org/10.1016/0013-4686(63)80042-0).
45. Lasia, A. (2014). *Electrochemical Impedance Spectroscopy and Its Applications* (Springer). <https://doi.org/10.1007/978-1-4614-8933-7>.
46. R Core Team (2019). R: a language and environment for statistical computing. <https://www.r-project.org/>.